Contents lists available at ScienceDirect

Physica E

journal homepage: www.elsevier.com/locate/physe

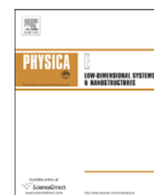

Characterization of InN epilayers grown on Si(111) substrates at various temperatures by MBE

Yan-Hsin Wang [a], Wei-Li Chen [b,*], Ming-Fei Chen [a]

[a] Department of Mechatronics Engineering, National Changhua University of Education, Taiwan 500, ROC
[b] Department of Electronic Engineering, National Changhua University of Education, Taiwan 500, ROC

ARTICLE INFO

Article history:
Received 2 April 2009
Received in revised form
10 June 2009
Accepted 10 June 2009
Available online 16 June 2009

PACS:
68.55.A−
61.72.Dd
68.37.−d
78.55.Cr

Keywords:
InN
Plasma-assisted molecular beam epitaxy
Atomic force microscope
X-ray diffraction
Transmission electron microscopy
Photoluminescence
Carrier concentrations
Hall mobility
Raman spectra

ABSTRACT

InN films have been grown by plasma-assisted molecular beam epitaxy (PAMBE) and characterized by various technologies. It was found that the structural, optical and electrical properties can be drastically improved by raising growth temperature from 440 to 525 °C. Grainy morphology was found in the grain size was found in atomic force microscope images. The large grain size was about 360 nm for a film grown at 525 °C. These films exhibited Wurtzite structure with a *c*/*a* ratio ranging from 1.59 to 1.609. The dislocation densities estimated by X-ray diffraction techniques closely agreed with those analyzed by plan-view transmission electron microscopy. Photoluminescence (PL) studies confirmed near band-to-band transitions and the narrowest low-temperature PL peak width was found to be 24 meV at 0.666 eV. Carrier concentrations decreased from 1.44×10^{19} to $1.66\times10^{18}\,cm^{-3}$ and Hall mobility increased from 226 to 946 $cm^2\,V^{-1}\,s^{-1}$ as the growth temperature is progressively increased from 440 to 525 °C. Raman spectra also indicated improved crystal quality as the growth temperature was raised.
© 2009 Elsevier B.V. All rights reserved.

1. Introduction

The epitaxial growth of InN is difficult because of low dissociation temperature and lack of suitable lattice-matched substrate materials. InN can decompose rapidly in vacuum as low as 430 °C [1]. The preferred high growth temperature to crack ammonia precursor for the growth of InN by metal organic vapor phase epitaxy (MOVPE) conflicts with the lower substrate temperature required to prevent dissociation. MOVPE growth of InN is not as successful as the growth of AlN and GaN. A much lower growth temperature is utilized by plasma-assisted molecular beam epitaxy (PAMBE) because of the use of nitrogen plasma. PAMBE has the advantage over MOVPE of employing lower growth temperature. The absence of a native substrate for the growth of InN requires a foreign substrate. Sapphire and silicon are commonly used for InN heteroepitaxy. It has been found that the initial treatments prior to the MBE growth of InN including AlN and low-temperature InN (LT-InN) buffer layer deposition play an important role in the quality of InN films [2,3]. The effects of buffer layer thickness, growth temperature, and flux ratio have been explored by many research teams [4–8].

Nevertheless, InN is a novel material for applications in future photonic and electronic devices. The band-gap energy of InN has been found to be around 0.7 eV according to optical characterization results [9–11]. It extends the operation wavelength of the III-nitride-based light-emitting devices to cover the spectrum range from near-infrared to ultraviolet (0.7–6.2 eV). InN is also a promising material for applications in high-speed devices such as high electron mobility transistors (HEMTs). It demonstrates highest peak drift velocity of all nitride semiconductors under high electrical field [12], and its relatively higher mobility (∼2000 $cm^2\,V^{-1}\,s^{-1}$) and lower concentration (∼1017 cm^{-3}) were measured at room temperature [13,14].

Important material parameters such as lattice constants, stress, constitutional material composition, grain size and crystalline direction can be analyzed by X-ray diffraction (XRD) [15,16].

* Corresponding author. Tel.: +886 4 7232105x7136; fax: +886 4 7211283.
E-mail address: weili@cc.ncue.edu.tw (W.-L. Chen).

1386-9477/$ - see front matter © 2009 Elsevier B.V. All rights reserved.
doi:10.1016/j.physe.2009.06.005

Recently, a lot of research groups have employed rocking curve analysis by high-resolution X-ray diffraction (HRXRD) to estimate the density of threading dislocations [15–19]. Lu et al. [20] and Liu et al. [21] investigated the optimized growth temperature of InN by measuring electrical, optical and XRD characteristics. This paper presents an investigation on the growth of InN layers on Si(1 1 1) substrates by plasma-assisted molecular beam epitaxy using different growth temperatures. We have examined the morphological, structural, electrical and optical characteristics to assess crystal quality of grown InN thin film.

2. Experimental procedure

The growth of InN films was conducted in an Oxford CLUSTERLAB 600 MBE system with a base pressure of 3×10^{-11} Torr. Active nitrogen was supplied by an Oxford Applied Research HD-25 radio frequency (RF) plasma source. Aluminum and indium fluxes were supplied by standard thermal effusion cells. Substrate temperature was measured by an SVT Associates In-Situ 4000 process monitor based on emissivity-corrected pyrometry. The emissivity was calibrated by the eutectic point of Si/Al alloy at 577 °C. Chamber pressure during growth was in the range of low 10^{-5} Torr. Si(1 1 1) substrates were ultrasonically cleaned using solvents. They were etched at 80 °C for 10 min in $NH_4OH{:}H_2O_2{:}H_2O = 1{:}1{:}5$ base solution to remove inorganic impurities followed by 10 min etch in $HCl{:}H_2O_2{:}H_2O = 1{:}1{:}6$ to remove metal ions. Substrates were dipped in buffered oxide etch (BOE) solution for 1 min to remove native oxide before loading into growth chamber. Immediately after being introduced into the growth chamber, the substrates were heated to 930 °C for 30 min to remove native oxide. A clean surface was confirmed by the appearance of Si(1 1 1) 7×7 reconstructed reflection high-energy electron diffraction (RHEED) patterns when the substrate temperature was reduced to around 750 °C. Prior to high-temperature InN (HT-InN) growth, an AlN buffer layer was grown at 850 °C for 7 min near stoichiometric flux condition. The aluminum beam equivalent pressure (BEP) was 3.3×10^{-7} Torr, and the plasma source was operated at 0.7 sccm nitrogen flow rate and 240 W RF power. The substrate was then lowered to 300 °C to grow a 20-nm-thick low-temperature InN buffer layer. The plasma source was operated using 0.5 sccm nitrogen flow rate and 200 W RF power. Higher temperatures (440, 475, 500 and 525 °C for sample A, B, C and D, respectively) were employed to grow HT-InN epilayer. The deposition rate was approximately 0.32 μm/h and the total thickness was ~0.5 μm. The indium BEP was 8.9×10^{-7} Torr, and the plasma source was operated at 1 sccm nitrogen flow rate and 240 W RF power to maintain flux ratio slightly nitrogen rich. Aluminum, indium and nitrogen fluxes were characterized by AlN and InN growth rates obtained by cross-sectional SEM images under metal-limited and nitrogen-limited growth conditions, respectively.

Surface morphology and roughness were measured by an NT-MDT Solver P47 AFM using the non-contact operation mode. A Siemens D5000 high-resolution X-ray diffraction system was used to determine the structural quality of grown films. A JEOL JEM-2010 TEM system was used for plan-view transmission electron microscopy (TEM) analysis. Phonon properties were characterized by Raman spectroscopy. Photoluminescence spectra were excited by a solid-state 532 nm laser.

3. Results and discussion

Fig. 1 shows the surface morphology of all samples. Surfaces reveal grain features of various sizes for samples grown at higher temperatures. The grain feature cannot be observed for sample A grown at 440 °C. The grain size of other samples increased when

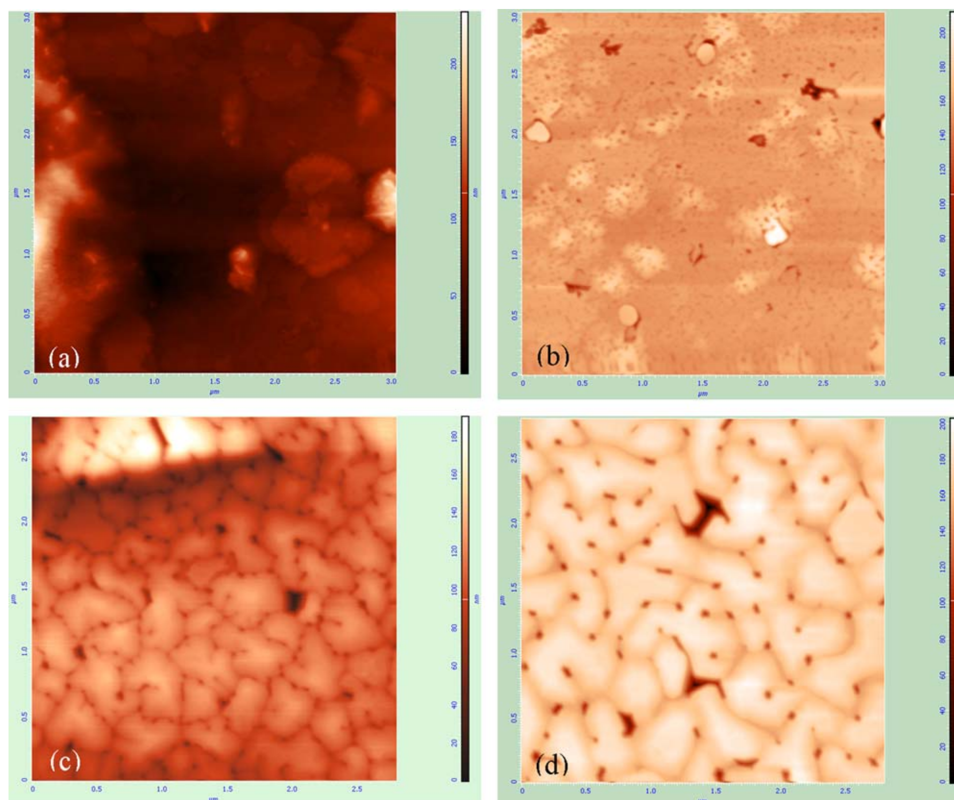

Fig. 1. Surface morphology of the AFM image ($2.79\times2.79\,\mu m^2$) of InN layers: (a) sample A; (b) sample B; (c) sample C and (d) sample D.

the growth temperature was raised. The largest grain size was 360 nm observed on the sample grown at 525 °C. In our system, further increasing growth temperature to 535 °C introduced InN dissociation and thus led to poor crystal quality accompanied by indium droplet formation. The dependence of grain size on growth parameters is listed in Table 1. Increased diffusion length of species on the growth front could facilitate the formation of larger grains. Faceted pits locating at grain boundaries are evident, which are commonly observed on InN grown under nitrogen-rich condition. Surface root mean square roughness measured are 2.76, 5.43, 28.29 and 15.06 nm for samples A, B, C and D, respectively. Deep trenches of 10–20 nm in depth separated grains. The depth of the faceted pits is over 50 nm. The higher surface roughness of samples C and D is contributed by deep trenches and pits. The automic force microscope (AFM) morphology and its line scan profiles indicated a smooth surface with terrace-type features on top of grains.

The lattice constant of InN thin film was measured by $(0\,0\,0\,2)$ and $(1\,0\,\bar{1}\,2)$ $2\theta/\omega$ scans. There was no indium-related peaks found in the scans. X-ray diffraction measurements showed that the c and a lattice parameters of InN were 5.701 ± 0.003 Å and 3.565 ± 0.021 Å, respectively. The resulted c/a ratios are 1.609, 1.602, 1.593 and 1.590 for samples grown at 440, 475, 500 and 525 °C, respectively. The decreasing c/a ratio indicated that films grown at higher temperature sustain relatively higher tensile strain.

The mosaic structure is usually characterized by its in-plane and out-of-plane components of the mosaic misorientation. Srikant et al. [22] determined the tilt and twist angles of mosaic structures from the full-width at half-maximum (FWHM) of symmetric and asymmetric ω-scans (rocking curves). The broadening of symmetric rocking curves, which is used to calculate tilt angle, includes the contribution from grain size effect. Therefore, the deduced tilt angle will be over-estimated. To separate the broadening from tilt and grain size, symmetric reflections of different reciprocal vector length were used by Williamson and Hall [23]. As the scattering order increases, the broadening in reciprocal space due to tilted planes also increases. However, the broadening contributed by grain size remains constant while the scattering order increases. Fig. 2 shows the rocking curve FWHMs of different plane sets with various inclination angles and their fitting curves following the procedures described in Ref. [22]. The twist angle can be extracted from the parameter of the fitting plot. Fig. 3 illustrates Williamson–Hall plots of InN epilayers and their linear fits. The tilt angle can be deduced from the slope of the plot. By assuming random dislocation distribution, edge-type dislocation density (N_E) and screw-type dislocation density (N_S) can be calculated by the following formula [24]:

$$N_E = \frac{\alpha}{4.35 b_e^2} \quad (1)$$

$$N_s = \frac{\beta^2}{4.35 b_s^2} \quad (2)$$

where α is the twist angle, β the tilt angle, b_e the length of edge-type Burgers vector and b_s the length of screw-type Burgers vector. Table 2 lists the calculated twist angles, tilt angles, edge and screw dislocation densities. The results indicate that about 90% of the dislocations are pure edge type or mixed type containing in-plane $[1\,1\,\bar{2}\,0]$ Burgers vectors. Fig. 4 shows the plan-view TEM images of samples C and D taken under $\mathbf{g} = [1\,1\,\bar{2}\,0]$ two beam condition. Only pure edge-type or mixed-type dislocations containing Burgers vectors $[1\,1\,\bar{2}\,0]$ can be observed. Pure screw-type dislocations with $\mathbf{b} = [0\,0\,0\,2]$ are invisible because $\mathbf{g} \cdot \mathbf{b} = 0$. The edge-type dislocation densities of samples C and D are 2.4 and $1.76 \times 10^{10}\,\mathrm{cm^{-2}}$, respectively. These values are smaller than those (3.3 and $2.27 \times 10^{10}\,\mathrm{cm^{-2}}$) estimated by XRD. AFM, XRD and TEM data all indicate that increasing HT-

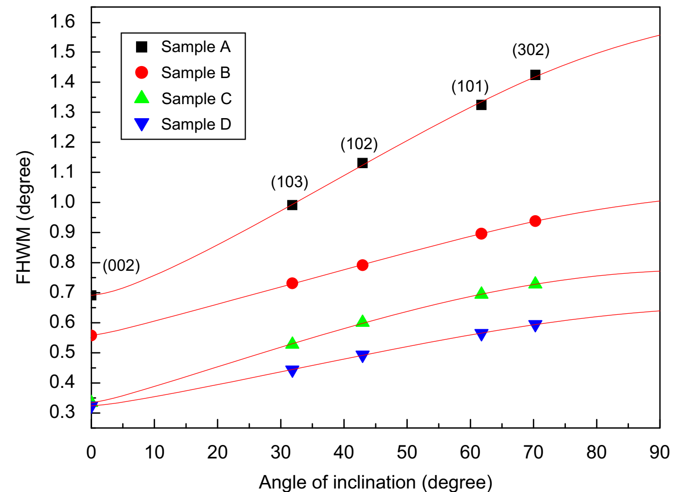

Fig. 2. Rocking curve FWHMs of plane sets with various inclination angles and their fitting curves.

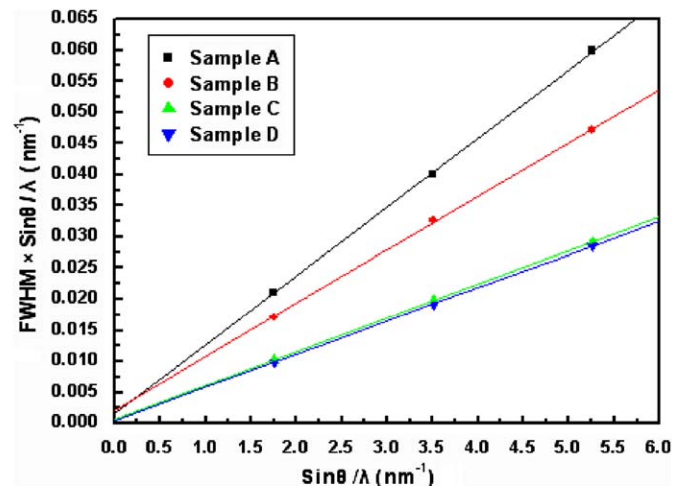

Fig. 3. Williamson–Hall plots of InN samples.

Table 1
The dependence of grain size on growth parameters for all samples.

Sample	A	B	C	D
Grain size	–	~80	~250	~360
HT-InN growth temperature (°C)	440	475	500	525
RF power			240 W	
Nitrogen flow			1 sccm	

Table 2
Screw-type and edge-type dislocation densities of all samples.

Sample	A	B	C	D
Tilt angle (deg.)	0.634	0.492	0.311	0.304
Twist angle (deg.)	1.544	0.995	0.769	0.637
Screw-type dislocation density ($\times 10^9\,\mathrm{cm^{-2}}$)	8.653	5.215	2.082	1.973
Edge-type dislocation density ($\times 10^{10}\,\mathrm{cm^{-2}}$)	13.33	5.542	3.304	2.27

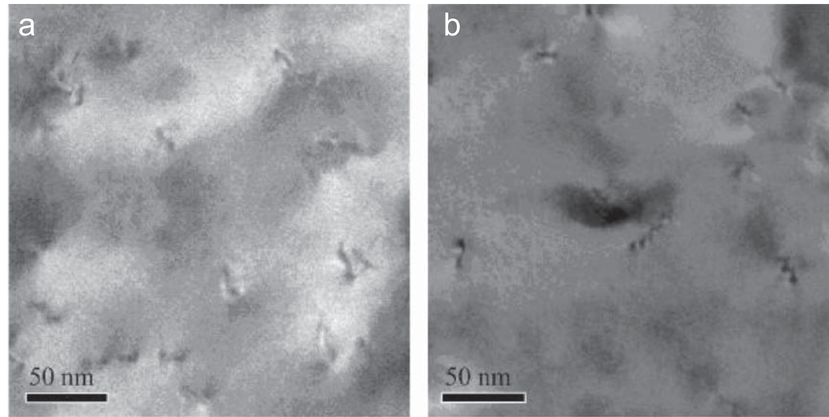

Fig. 4. Plan-view TEM images of (a) sample C and (b) sample D. The threading dislocation densities are 2.4 and $1.76\times10^{10}\,cm^{-2}$, respectively.

InN growth temperature results in larger grain size and lower threading dislocation density.

Optical property of InN samples was characterized by photoluminescence. The PL setup consisted of a 532 nm solid-state laser and its maximum power was about 130 mW. InN grown at higher temperature showed stronger luminescence intensity and increasingly narrower peak width. The sample with highest growth temperature showed best optical performance and its low-temperature (15 K) PL spectrum peak position was at 0.666 eV with 24 meV FWHM fitted by Gaussian function. There was no luminescence feature found near 1.9 eV.

The exciting power was changed from 0.5 to 98 mW to study power-dependent photoluminescence of sample B at 15 K. The integrated PL intensities under various excitation levels are plotted in Fig. 5. They are found to vary linearly with the excitation intensity without saturation over more than two orders of magnitude, which is consistent with the direct band-to-band emission nature [25]. As shown in the inset of Fig. 6, the transition peak shifted from 0.65 eV at low excitation to 0.657 eV at high excitation. Both band-filling effects introduced quasi-Fermi level increase in conduction band [26], and the effect of Urbach tail slightly above valence band [27] can lead to blue shift in transition peak. Because PL peak position quickly increased by 4 meV with pumping intensity increased from 0.17 to 4.71 mW and then it gradually increased and saturated at high excitation, we attribute the increase of transition energy as the effect of low-density Urbach tail near valance band.

Temperature-dependent photoluminescence has been done in the temperature range from 12 to 300 K to explore the temperature dependence of excitonic transition energy of sample A. The result is plotted in Fig. 6. The energy peak initially shows a blue shift and then reaches a maximum value followed by a red shift when the temperature is further lowered. If the temperature is further decreased, the peak energy shows blue shift again. The rate of blue shift at high- and low-temperature ranges is ~0.2 meV/K, which is consistent with the rate of bandgap shrinkage due to temperature change. The s-shaped peak position versus temperature is illustrated in the inset of Fig. 6. The highest transition peaks occurred at 225, 150, 125 and 110 K for samples A, B, C and D, respectively. Since both morphology and XRD analysis data indicate that larger grains, less grain boundaries and lower dislocation densities are associated with films of better quality, we speculate the unusual phenomenon might be related to defects at grain boundary. Detailed optical analysis is currently under study to clarify the mechanism.

The temperature-dependent Hall mobility and carrier density were determined by Hall measurements with van der Pauw

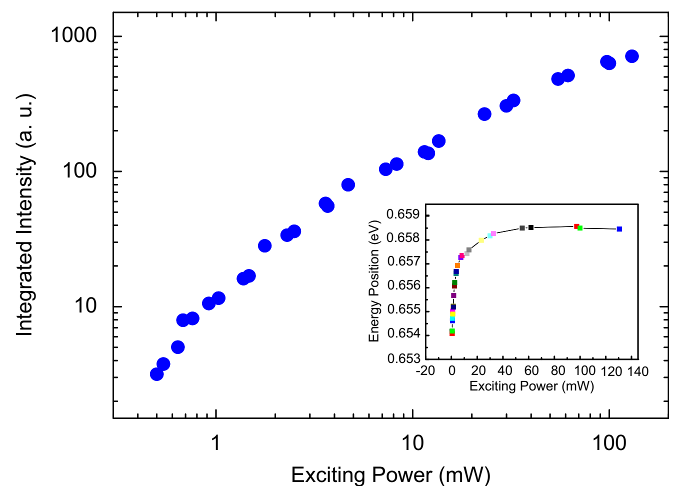

Fig. 5. Power-dependent PL spectra of sample B at 15 K. The near band-to-band transition is confirmed by the observation that the integrated luminescence intensity increases linearly with excitation power. A 7 meV blue shift in luminescence peak is observed as the excitation power is increased over two orders as shown in the inset. The quick increase of transition energy at low excitations is due to the Urbach tail.

configuration. As illustrated in Fig. 7, carrier concentration decreases and Hall mobility increases as the HT-InN growth temperature is progressively increased from 440 to 525 °C. The best results are obtained on sample D with a carrier concentration of $1.74\times10^{18}\,cm^{-3}$ and a mobility of $946\,cm^2\,V^{-1}\,s^{-1}$ at room temperature.

Raman spectrum was conducted by using a 532 nm excitation source. The experiment was done using a $Z(XX)\bar{Z}$ geometry. Z is parallel to the sample surface plane normal. Only E_2 and A_1(LO) modes can be observed in this configuration. The peak position corresponding to InN E_2^{high} was close to $489\,cm^{-1}$ and it was near $587\,cm^{-1}$ for A_1(LO). These values agreed with previously reported results [28]. The amount of Raman shift and the associated peak width of InN are plotted in Fig. 8. The improvement in E_2^{high} peak width confirmed that an improvement in crystalline quality can be achieved by raising the growth temperature of HT-InN [29].

4. Conclusions

The growth temperature influence on the structural, morphological, electrical and optical characteristics of InN thin films have

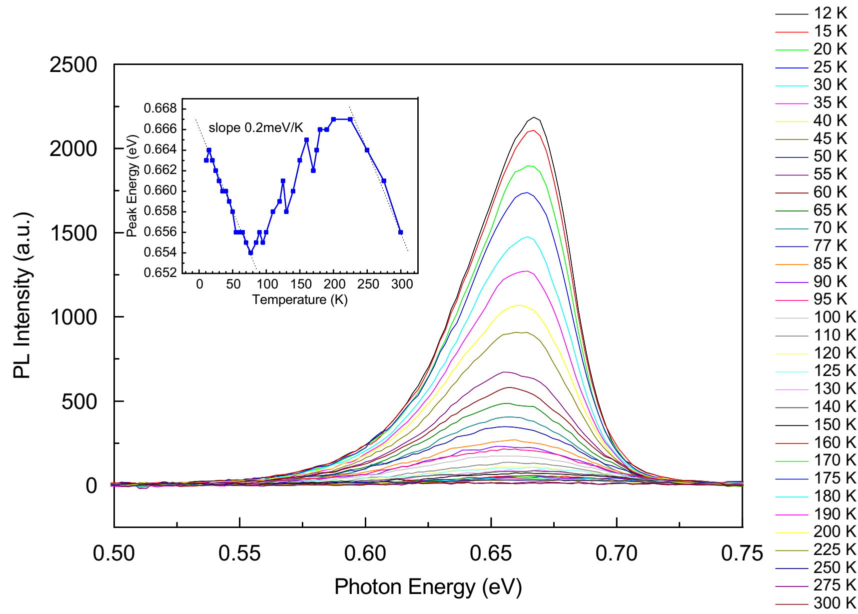

Fig. 6. PL peak position vs. temperature of InN samples.

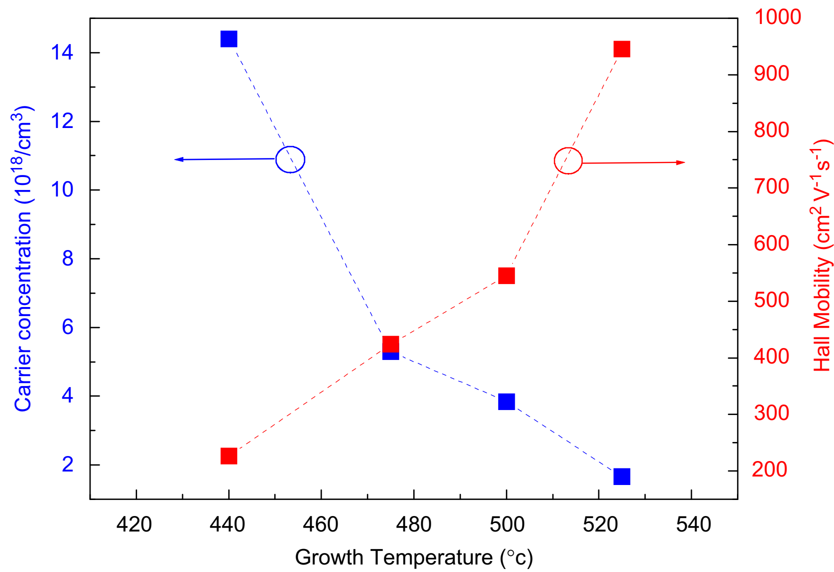

Fig. 7. Carrier concentration and mobility of InN samples measured by Hall experiment at 300 K.

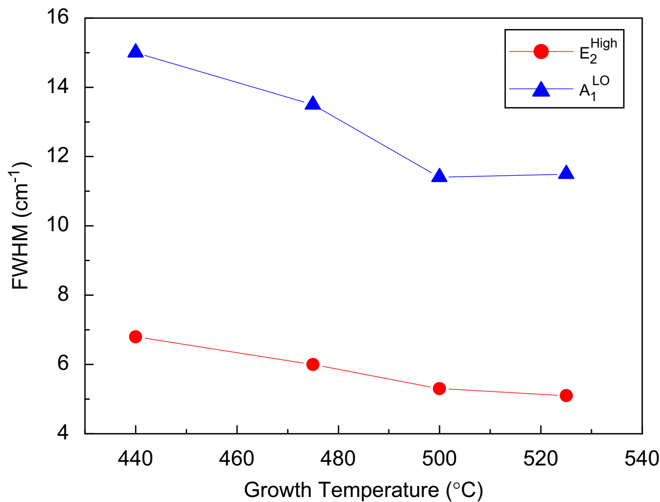

Fig. 8. Raman spectrum of InN samples.

been studied. Higher growth temperature resulted in better material quality, as evidenced by increased grain size, lower defect density, narrower luminescence and Raman shift peak width. As growth temperature was increased from 440 to 525 °C, Hall mobility increased from 226 to 946 $cm^2 V^{-1} s^{-1}$ while carrier concentration decreased from 1.44×10^{19} to 1.66×10^{19} cm^{-3}. PL measurement indicated near band-to-band transition nature and the low-temperature band-edge transition of InN grown at 525 °C was 0.666 eV. Both XRD and plan-view TEM studies confirmed that the dominating threading dislocation was edge type. The edge-type dislocation density for samples grown at 500 and 525 °C were 2.24 and 1.44×10^{10} cm^{-2}, respectively.

Acknowledgements

We would like to express sincere thanks to Y.C. Chen, Y.K. Huang and K.D. Wu for their contributions in this work.

References

[1] W.-L. Chen, R.L. Gunshor, Jung Han, K. Higashimine, N. Otsuka, MRS Internet J. Nitride Semicond. Res. 5S1 (2000) W3.30.
[2] Y. Nanishi, Y. Saito, T. Yamaguchi, Jpn. J. Appl. Phys. 42 (2003) 2549.
[3] C.-L. Wu, C.-H. Shen, H.-Y. Chen, S.-J. Tsai, H.-W. Lin, H.-M. Lee, S. Gwo, T.-F. Chuang, H.-S. Chang, T.M. Hsu, J. Cryst. Growth 288 (2006) 247.
[4] Y. Saito, T. Yamaguchi, H. Kanazawa, K. Kano, T. Araki, Y. Nanishi, N. Teraguchi, A. Suzuki, J. Cryst. Growth 237–239 (2002) 1017.
[5] J. Grandal, M.A. Sanchez-Garcia, J. Cryst. Growth 278 (2005) 373.
[6] H. Ahn, C.-H. Shen, C.-L. Wu, S. Gwo, Thin Solid Films 494 (2006) 69.
[7] C.-L. Wu, C.-H. Shen, H.-Y. Chen, S.-J. Tsai, H.-W. Lin, H.-M. Lee, S. Gwo, T.-F. Chuang, H.-S. Chang, T.M. Hsu, J. Cryst. Growth 288 (2006) 247.
[8] T. Yamaguchi, M. Kurouchi, H. Naoi, A. Suzuki, T. Araki, Y. Nanishi, J. Cryst. Growth 275 (2005) e1321.
[9] V.Yu. Davydov, A.A. Klochikhin, R.P. Seisyan, V.V. Emtsev, S.V. Ivanov, F. Bechstedt, J. Furthmuller, H. Harima, A.V. Mudryi, J. Aderhold, O. Semchinova, J. Graul, Phys. Status Solidi B 229 (2002) R1.
[10] J. Wu, W. Walukiewicz, K.M. Yu, J.W. Ager III, E.E. Haller, H. Lu, W.J. Schaff, Appl. Phys. Lett. 80 (2002) 4741.
[11] Fei Chen, A.N. Cartwright, Hai Lu, William J. Schaff, Physica E 20 (2004) 308.
[12] A.G. Bhuiyan, A. Hashimoto, A. Yamamoto, J. Appl. Phys. 94 (2003) 2779.
[13] N. Grandjean, J. Massies, M. Leroux, Appl. Phys. Lett. 69 (1996) 2071.
[14] S.C. Jain, M. Willander, J. Narayan, R. Van Overstraeten, J. Appl. Phys. 87 (2000) 965.
[15] J. Gwóʹzdʹz, B. Grushko, M. Surowiec, Mater. Sci. Eng. A 294–296 (2000) 49.
[16] B. Liu, R. Zhang, Z.L. Xie, H. Lu, Q.J. Liu, Z. Zhang, Y. Li, X.Q. Xiu, P. Chen, P. Han, S.L. Gu, Y. Shi, Y.D. Zheng, W.J. Schaff, J. Appl. phys. 103 (2008) 023504.
[17] Z.T. Chen, K. Xu, L.P. Guod, Z.J. Yang, Y.Y. Su, X.L. Yang, Y.B. Pan, B. Shen, H. Zhanga, G.Y. Zhang, J. Cryst. Growth 294 (2006) 156.
[18] Y. Huang, H. Wang, Q. Sun, J. Chen, D.Y. Li, J.C. Zhang, J.F. Wang, Y.T. Wang, H. Yang, J. Cryst. Growth 293 (2006) 269.
[19] X. Wang, S.-B. Che, Y. Ishitani, A. Yoshikawa, Appl. Phys. Lett. 99 (2007) 151901.
[20] Hai Lu, William J. Schaff, Jeonghyun Hwang, Hong Wu, Wesley Yeo, Amit Pharkya, Lester F. Eastman, Appl. Phys. Lett. 77 (2000) 2548.
[21] Bin Liu, Rong Zhang, Zi-Li Xie, Xiang-Qian Xiu, Liang Li, Jie-Ying Kong, Hui-Qiang Yu, Pin Han, Shu-Lin Gu, Yi Shi, You-Dou Zheng, Chen-Guang Tang, Yong-Hai Chen, Zhan-Guo Wang, Sci. China Ser. G 51 (2008) 237.
[22] V. Srikant, J.S. Speck, D.R. Clarke, J. Appl. Phys. 82 (1997) 4286.
[23] G.K. Williamson, W.H. Hall, Acta Metall. 1 (1953) 22.
[24] P. Gay, P.B. Hirsch, A. Kelly, Acta Metall. 1 (1953) 315.
[25] S. Gwo, C.-L. Wu, C.-H. Shen, W.-H. Chang, T.M. Hsu, J.-S. Wang, J.-T. Hsu, Appl. Phys. Lett. 84 (2004) 3765.
[26] Fei Chen, A.N. Cartwrighta, Hai Lu, William J. Schaff, Physica E 20 (2004) 308.
[27] X. Wang, S.-B. Che, Y. Ishitani, A. Yoshikawa, Appl. Phys. Lett. 90 (2007) 201913.
[28] V. Yu. Davydov, V.V. Emtsev, I.N. Goncharuk, A.N. Smirnov, V.D. Petrikov, V.V. Mamutin, V.A. Vekshin, S.V. Ivanov, M.B. Smirnov, T. Inushima, Appl. Phys. Lett. 75 (1999) 3297.
[29] M. Kuball, Surf. Interf. Anal. 31 (2001) 987.